PAPER

Check for updates

Conductivity and giant permittivity study of Zn$_{0.5}$Ni$_{0.5}$Fe$_2$O$_4$ spinel ferrite as a function of frequency and temperature

Mohsen Elain Hajlaoui,[ab] Radhia Dhahri,[a] Nessrine Hnainia,[b] Aida Benchaabane, [cd] Essebti Dhahri[a] and Kamel Khirouni[e]

Ni$_{0.5}$Zn$_{0.5}$Fe$_2$O$_4$ was prepared by the solid state reaction route at different temperatures. The dielectric properties of spinel ferrites were investigated in the frequency range 50 Hz–10 MHz and in the temperature range 300–420 K. Conductance is shown to increase with increasing frequency and temperature. Impedance analyses indicated that the relaxation phenomenon is strongly dependent on temperature and frequency. The impedance plots displayed both intra- and inter-granular contributions. Electrical equivalent circuit was proposed to explain the impedance results. The decrease of giant permittivity values with the increase in frequency proves the dispersion in the low frequency range and is showing the Maxwell–Wagner interfacial polarization.

Introduction

In recent years, spinel ferrite materials have attracted the interest of scientists, especially synthetic chemists[1–3] because of their application in several disciplines such as biomedicine,[4] catalysis,[5] and magnetic resonance imaging.[6] Among the diverse spinel ferrites Zn–Ni ferrites are found to be very attractive for the modern electronics industry due to high mechanical strength, good chemical stability, high magnetic permeability and resistivity.[3,7,8] In order to prepare these ferrite nanomaterials, different methods have been reported, such as co-precipitation,[9] sol–gel combustion,[10] hydrothermal[11] and ball milling methods.[12] Moreover, spinel ferrites Ni$_{0.5}$Zn$_{0.5}$Fe$_2$O$_4$ are best known for their low dielectric loss, large permeability, high electric resistivity and unique magnetic structure.[13] Due to these properties they are widely used in electronics devices such as magnetic heads, magnetic resonance imaging, filters,[14] gas sensors,[15–17] super capacitors and fuel cells.[18,19] Hence it is challenging to prepare magnetic nanoparticles with bulk magnetic properties. Moreover, ferrite microstructures highly

depend on the preparation process where annealing temperature affects magnetic and electric properties. In this context, many reports covered the structural and magnetic properties of Ni–Zn systems.[20–23] The study of the electric properties, however, is still ongoing.

This work aims to investigate the dielectric properties of Zn$_{0.5}$Ni$_{0.5}$Fe$_2$O$_4$ ferrite system a wide frequency (50 Hz–10 MHz) and temperature (300–420 K) range by using X-ray diffraction and impedance spectroscopy. We deduce the transport mechanism involved in dc and ac conductance. Both conductance and activation energy values of our samples as a function of temperature and frequency are established.

Experimental

Nickel–zinc ferrites Ni$_{0.5}$Zn$_{0.5}$Fe$_2$O$_4$ were synthesized using solid-state reaction technique. Powder of the oxides NiO, ZnO and Fe$_3$O$_4$ with above 99.9% purity were mixed and pressed into pellets with 8 mm of diameter and 1.2 mm of thickness. Finally, the samples were sintered for 24 h at 1000 °C then heated at 1200 °C for 12 h to obtain the homogeneity of the compound.

The homogeneity, the phase purity, lattice structure and cell parameters of the ferrites nanoparticles was checked by XRD technique using X-ray diffractometer (Siemens D5000 X-ray diffractometer) with monochromatized Cu-Kα radiation λ_{Cu} = 1.5406 Å radiation.

In order to prepare the sample for electrical characterization, we have achieved to deposit, on each side of the pellet, an aluminum layer of 200 nm thickness using thermal heat evaporation under vacuum. To prevent solvent infiltration into the paint, a gold wire is attached to the aluminum layer by a silver paint. Electrical and dielectric data over large temperature

[a]Laboratoire Physique Appliquée, Faculté des Sciences, Université de Sfax, B. P. 1171, Sfax 3000, Tunisia. E-mail: elain.hajlaoui@istmt.utm.tn

[b]Laboratoire des Nanomatériaux et de Systèmes pour les Energies Renouvelables Centre de Recherches et des Technologies de l'Energie, Technopole Borj Cedria, BP 095 Hammam Lif, Tunisia

[c]Laboratoire Matériaux Avancés et Phénomènes Quantiques, Faculté des Sciences de Tunis El Manar, Campus Universitaire, Université Tunis El-Manar, 2092 Tunis, Tunisia

[d]Laboratoire de Physique de la Matière Condensée, UFR des Sciences d'Amiens, 80039 Amiens, France

[e]Laboratoire de Physique des Matériaux et des Nanomatériaux Appliqués à l'Environnement, Faculté des Sciences de Gabès, 6079 Gabès, Tunisia

range were recorded through an Agilent 4294A impedance analyzer, whose frequency scale is of 40 Hz–110 MHz. For completely excluding the effects of sun shine and other sources of lights, the measurements were conducted under dark.

Results and discussion

From X-ray diffractogramme, it is clear that the synthesized compound is single phase (Fig. 1). The Rietveld refinements of the XRD data performed using Fullprof program[24] revealed that this compound crystallizes in the cubic structure with the *Pm3m* space group in which $\alpha = 8312$ Å and $V = 586.631$ Å^3. Fig. 2 show the structure of $Ni_{0.5}Zn_{0.5}Fe_2O_4$. The average particle size D_{SC} was calculated using Scherrer's formula:[25]

$$D_{SC} = \frac{(0.9 \times \lambda)}{(\beta \times \cos \theta)} \quad (1)$$

where λ is the used wavelength ($\lambda_{CuK\alpha} = 1.5406$ Å), θ and β are the Bragg angle and the full width at half maximum after subtracting the instrumental line broadening, respectively, for the most intense diffraction peak:

$$\beta = \left(\beta_m^2 - \beta_i^2\right)^{\frac{1}{2}} \quad (2)$$

where $\beta_m{}^2$ is the experimental full width at half maximum (FWHM) and $\beta_i{}^2$ is the FWHM of a standard silicon sample. The D_{SC} value of our sample is about 72 nm.

Fig. 3 exhibits the variation of conductance as a function of frequency at different temperatures. This physical entity is expressed by the following relation:

$$G = \sigma \frac{A}{l} \quad (3)$$

where σ is the conductivity, A is the cross-sectional area of the material and l is its length. We can distinguish two regions. For low frequencies (50 Hz to 10^3 Hz) we notice poor conductance dependence on frequency, contrarily to the strong dependence behavior on temperature seen from the same spectra. Such behavior can be explained by the Maxwell–Wegner two-layer
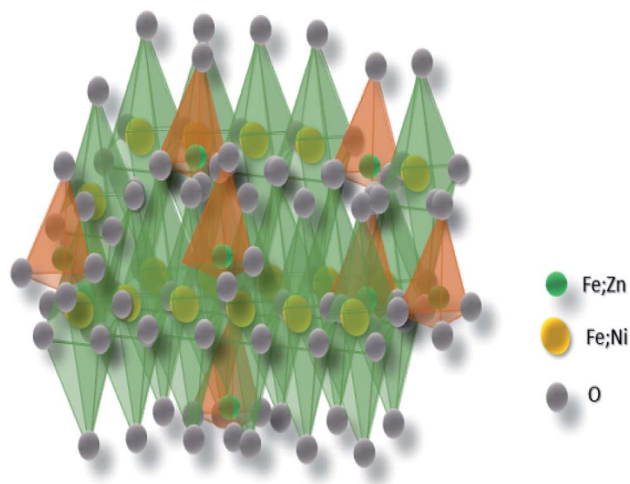

Fig. 2 Representation of $Ni_{0.5}Zn_{0.5}Fe_2O_4$. The octahedral sites are shown in green and the tetrahedral sites are in orange.

model suggesting that ferrites are made of well conducting grains surrounded by poorly conducting grain boundaries that are more active at lower frequencies. This leads to poor conductance resulting from weak electron hopping in the region.[26] The second region that spreads from 10^3 Hz to 10^6 Hz presents a significant increase of conductance with rising frequency and can be described by the power law:[7]

$$G(\omega) = A(\omega)^s \quad (4)$$

where A is a constant, ω is the angular frequency and the exponent s is the slope of the frequency dependent region $0 \leq s \leq 1$. Where s depends on the temperature and binding energy.[27]

Fig. 4 exhibits the variation of conductance with temperature. Shown in green and the tetrahedral sites are in orange.

It is well known that conduction in ferrites is led by the hopping of charge carriers between the sites.[28]

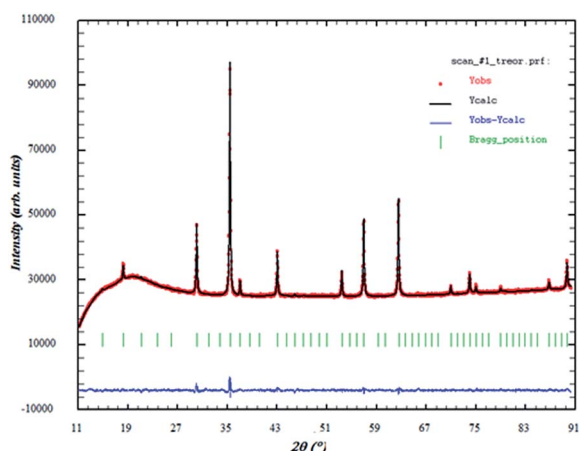The mechanism can be defined by the following equation:[29]

Fig. 1 Observed (circle), calculated (continuous line) and difference patterns (at the bottom) of X-ray diffraction data for $Ni_{0.5}Zn_{0.5}Fe_2O_4$.
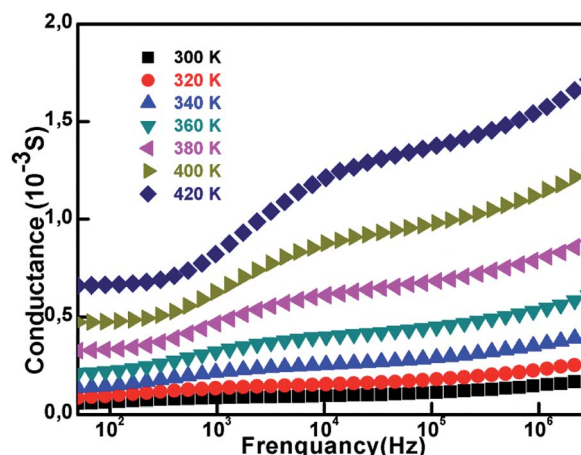

Fig. 3 Conductance as a function of frequency at different temperatures.
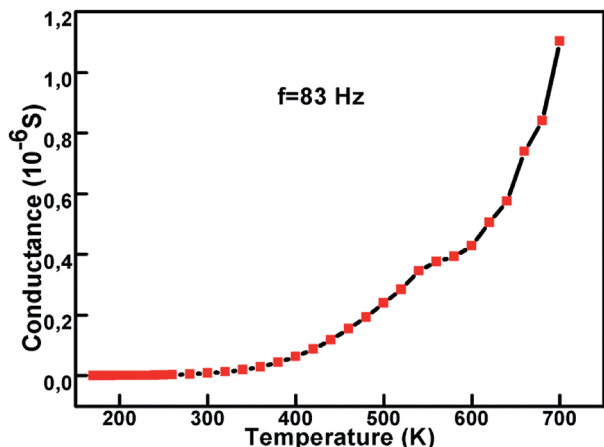
Fig. 4 Variation of conductance as function of temperature at $f = 83$ Hz.

$$G = \frac{B}{T}e^{-\frac{E_a}{k_B T}} \tag{5}$$

where B is a constant, T is the absolute temperature, E_a is the activation energy and k_B is Boltzmann constant. We observe an increase of conductance with the rise of temperature at fixed frequency (83 Hz). This is due to an increase of hopping phenomenon with the increase of temperature. As clearly seen the rise is more pronounced at 700 K and the graph shows semiconducting behavior[30] described by the increase of conduction with temperature. The linear relation between $\log(G.T)$ and 1000 T^{-1} confirms the temperature dependence of conduction at 83 Hz. In fact, the Arrhenius fit given by the eqn (5) as shown in Fig. 5 allows to obtain the activation energy which equal to 0.244 eV. This linear behavior clearly observed in the plot indicates that the conduction is due to electron hopping from Fe^{3+} to Fe^{2+} ions through the crystal lattice.[30] Whereas the value of the activation energy suggests a high potential barrier that can increase the difficulty of charge carriers mobility and thus affects the conduction mechanism. Rahmouni *et al.*[23] have reported a decrease in the value of
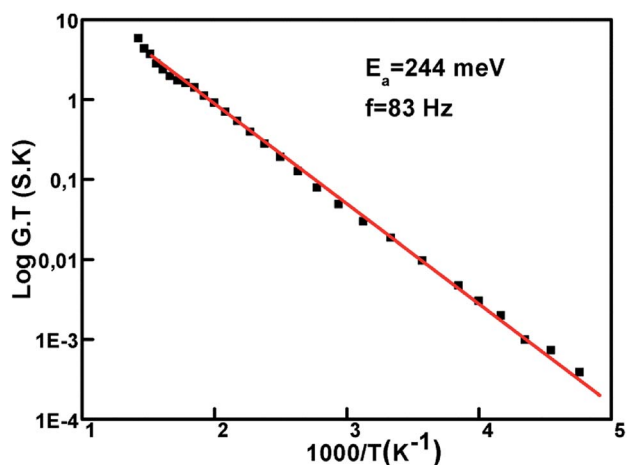
activation energy based on the nickel concentration where it went from 0.665 eV for $x = 0$ to 0.280 eV for $x = 0.5$. Thus, nickel ions concentration plays leading role in conduction mechanism same as temperature and high frequency. The actual part of the impedance measures the resistance of the circuit to the alternating current.

Fig. 6 presents the variation of Z' as function of frequency and by varying temperature from 300 K to 420 K with a step of 20 K each time. We also notice the presence of two zones, the first one is limited from 5×10^3 Hz and the second one beginning from 10^6. As we may see in the plot, for low temperatures and low frequencies the impedance values are elevated, and they decrease significantly for higher temperatures range. These values illustrate the temperature dependency behavior of conduction that directly affects the resistance. The alternating current resistance diminishes with the rising conduction at high temperatures. In fact, the remarkable change is attributed to the decrease of the potential barrier that creates free charge carriers. At high frequencies, we notice an acute decay of impedance that could be explained with the presence of a space-charge region resulting from the decline of charge barrier under the influence of temperature.[30] It is known that grain boundaries are active interfaces for the creation of such region.[31] Indeed, we can clearly observe constant values for Z' at different temperatures for low frequencies suggesting an accumulation of charge carriers at the grain boundaries.[32]

The variation of frequency dependent Z'' at varying temperature is shown in Fig. 7. We note that Z'' decrease when temperature increase. The plot indicates the presence of two peaks, called relaxation frequencies. The first peak, located between 50 Hz and 10^3 Hz depending on the temperature, is attributed to the grain boundaries. Whereas the second one placed between 10^5 Hz and 10^7 Hz is attributed to the relaxation of the grain boundary. In fact, we can notice the shift towards higher frequencies as the temperature increases. This tendency indicates that charge carriers are thermally activated[33] and are accumulated at the grain boundaries, and further confirms the semiconducting behavior of the nickel ferrites.
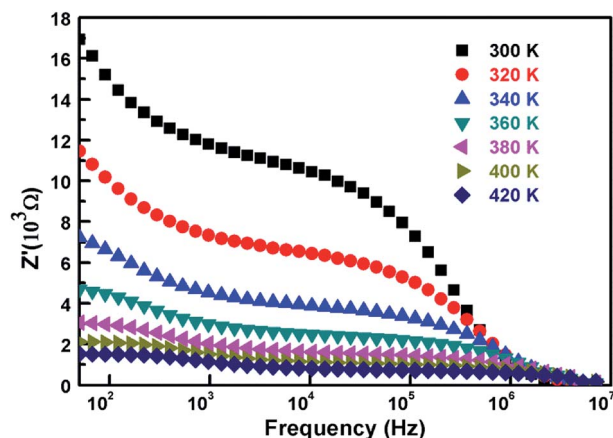

Fig. 5 Variation of $\log(G.T)$ with 1000 T^{-1} for $x = 50\%$.

Fig. 6 Variation of real impedance Z' with frequency at different temperatures.
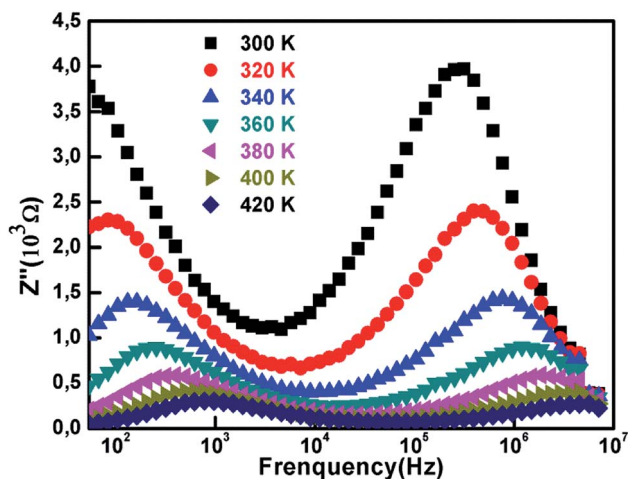
Fig. 7 Variation of imaginary impedance Z'' with frequency at different temperatures.

On the other side, the resistance is very low and keeps decreasing with the rising heat. Furthermore, for the frequency range around 10^6 we can clearly observe the merging of Z'' regardless of temperature, which indicates the decrease of space charge polarization.[34]

In order to determine the value of maximum frequency $f_{\max}$ for which the imaginary impedance has maximum value, we superposed both Z' and Z''. We observe the presence of two pics which correspond respectively to the two inflexion points for Z' and two maximums for Z''. The frequency $f_{\max}$ corresponds to the projection of the inflexion point on the frequency axis. For this case we have two inflexion points providing two maximums in agreement with the results discussed in the paragraph above.

Thus, from Fig. 8 we conclude the values of $f_{\max} = 92.6$ Hz and $f_{\max} = 782.4 \times 10^5$ Hz.

The plot of normalized imaginary part of impedance $\dfrac{Z''}{Z''_{\max}}$ as a function of normalized frequency $\dfrac{f}{f_{\max}}$ is exhibited in Fig. 9.
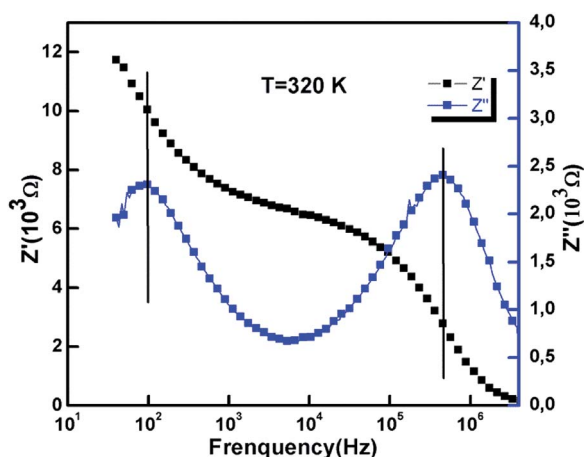

Fig. 8 Frequency dependence of real and imaginary parts of impedance Z' and Z'' at 320 K.
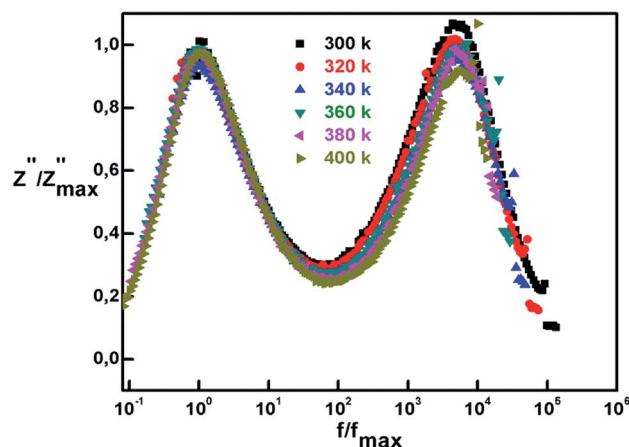

Fig. 9 $\dfrac{Z''}{Z''_{\max}}$ *vs.* $\dfrac{f}{f_{\max}}$ plots of nickel ferrites at different temperatures.

The representation aims to enable the study of dielectric relaxation. We observe an overlap of spectra into a master curve which denotes that relaxation process is irrespective to temperature. In fact, the temperature independency indicates the existence of one relaxation mechanism[35] for all spectra and the merging behavior could be explained by the emission of space charge.[36] Moreover, the value of full width at half maximum is found to be > 1.14 decades indicating a polydisperse non-exponential relaxation. This non-Debye (non-exponential) relaxation type may refer to a hopping mechanism of charge carriers along with time dependent mobility of the same type of charge carriers.[37] To ground deeper explanation to this phenomenon we refer to the following relation defining the non-Debye relaxation:[38]

$$\varphi(t) = \exp\left[-\left(\frac{t}{\tau}\right)^{\beta}\right] \quad ; (0 < \beta < 1) \tag{6}$$

where $\varphi(t)$ is the time evaluation of electric field, τ is the relaxation time at peak and β is the Kohlrausch exponent. The smaller value of β indicates larger deviation of relaxation with respect to Debye type relaxation where $\beta = 1$. To calculate the relaxation time from Z'' *vs.* $\log f$ plot, we use the following relation:[39]

$$\tau = \frac{1}{\omega} = \frac{1}{2\pi f_{\max}} \tag{7}$$

where $f_{\max}$ is the relaxation frequency. Logarithmic representation of relaxation frequency as a function of inverse temperature is shown in Fig. 10.

As discussed above we conclude that the relaxation frequency is increasing with temperature. The two slopes, attributed to the two frequencies observed in the impedance spectra, are used to determine the values of activation energies. Following the Arrhenius law:

$$f_{\max} = f_0 \, e^{-\frac{E_a}{k_B T}} \tag{8}$$

where $f_{\max}$ is the relaxation frequency, f_0 is the pre-exponential term and k_B is the Boltzmann constant. We obtain activation energy values of 0.250 eV and 0.228 eV corresponding
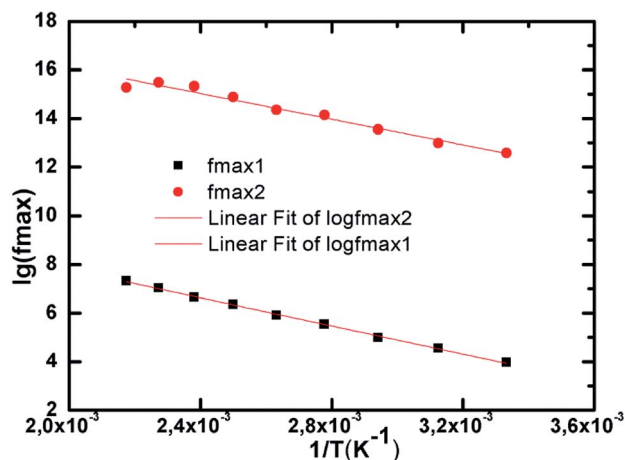
Fig. 10 Arrhenius plots for logarithmic representation of frequency as a function of 1/T.

respectively to the grain and the grain boundaries. Comparing the reported results from conduction and impedance spectra shows close values referring to the same hopping mechanism of charge carriers.[23]

Fig. 11 exhibits the plots of imaginary part as a function of real part of complex impedance at various temperatures of $Ni_{0.5}Zn_{0.5}Fe_2O_4$. This technique aims to investigate the contribution of grains and grain boundaries based on the frequency range. The plots present two semicircular arcs that are not centered on the axis of real impedance Z' indicating a non-Debye type of relaxation as previously concluded, and the obedience to Cole–Cole formalism.[40] For complex impedance it is given by the following relation:

$$Z^*(\omega) = \frac{R}{1 + \left(\frac{j\omega}{\omega_0}\right)^{1-n}} \qquad (9)$$

For when $n \to 0$ it results in the classical Debye's formalism. The decentralization could also explain the presence of only one electrical conduction mechanism.[41] In fact, we can attribute the low
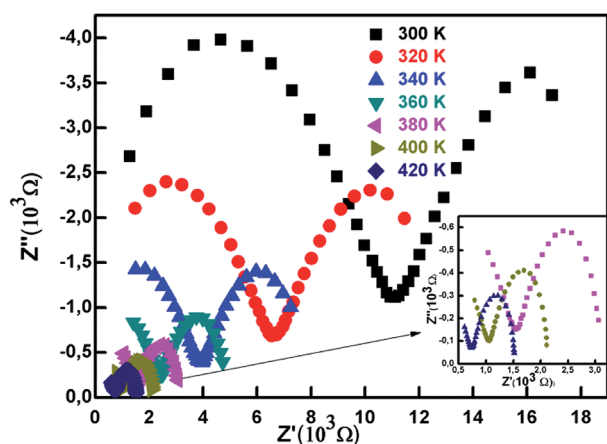
frequency semicircle to the grain contribution, whereas the second semicircle is attributed to the grain boundaries contribution.

The formation of two semicircular arcs suggests the existence of two types of relaxation phenomena with the relaxation time given by $\tau\omega_{max} = 1$, where τ is the relaxation time and ω_{max} is the relaxation pulsation. As a matter of fact, these results correspond to the findings reported in the previous paragraphs.

On the other hand, we note that the interception of the plots shifts toward lower values of Z' as the temperatures increases. There is a gradual decrease of resistance while the temperature is rising. This behavior indicates the low grain resistance for high temperatures, and the appearance of semicircles is indicative of semiconducting behavior.[41]

Using Z view software, we have simulated the plots of Z'' vs. Z'. Fig. 12 is showing the simulation accompanied with the equivalent circuit used for the $Ni_{0.5}Zn_{0.5}Fe_2O_4$ sample. The model contains a series of three R-CPE combination circuits where R is the resistance, and CPE is the constant phase element referring to the complex element. The combinations are attributed to grains and grain boundaries. The constant phase element impedance is defined by the following equation:[42]

$$Z_{CPE} = [A(J\omega)^{\alpha}]^{-1} \qquad (10)$$

where A is a proportional factor, ω is the angular frequency and α is the exponent between 0 and 1. At $\alpha = 1$ the constant phase element is considered an ideal capacitive element, whereas for $\alpha = 0$ it is equivalent to resistance.

Using the relationship $R = Z'/2$ we calculated the resistance in order to further investigate the relaxation phenomena and the conduction distribution.

Table 1 presents the values of resistance R and constant phase element CPE for each series at different temperature.

This data was used to draw the curve given in Fig. 13 showing the variation of resistance as a function of temperature. We can notice a sharp decrease of resistance between 300 K and 340 K more pronounced for $R1$ than $R2$ and $R3$, thereafter it starts
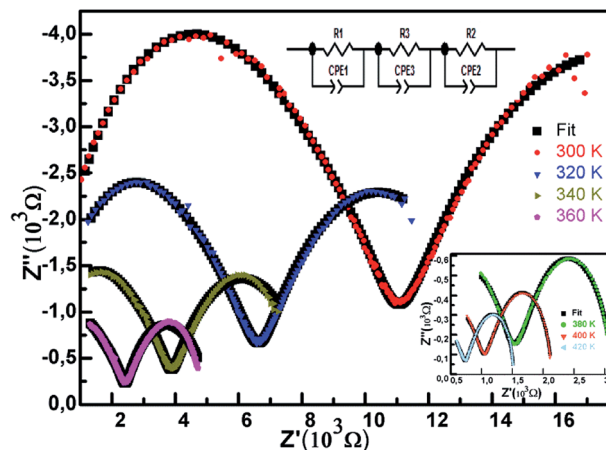

Fig. 11 Complex impedance spectrum for different temperatures.

Fig. 12 Nyquist diagram of $Ni_{0.5}Zn_{0.5}Fe_2O_4$ as a function of temperature. The inset showing the equivalent circuit.

Table 1 Variation of impedance parameters at various temperatures

Temperature (K)	R1 (Ω)	CPE1T (F)	CPE1P (F)	R2 (Ω)	CPE2T (F)	CPE2P (F)	R3 (Ω)	CPE3T (F)	CPE3P (F)
300	16 161	312×10^{-6}	0.59627	4382	$11\ 332 \times 10^{-8}$	0.76477	6377	1320×10^{-10}	0.95868
320	7412	1726×10^{-6}	0.69692	2956	$27\ 092 \times 10^{-8}$	0.70014	3695	1390×10^{-10}	0.962
340	4088	$14\ 846 \times 10^{-6}$	0.74431	1626	$13\ 597 \times 10^{-7}$	0.61015	2406	1912×10^{-10}	0.943
360	2259	$10\ 538 \times 10^{-6}$	0.8178	778.7	$32\ 877 \times 10^{-6}$	0.46832	1912	5821×10^{-10}	0.86629
380	1189	$76\ 433 \times 10^{-7}$	0.89876	529	$11\ 626 \times 10^{-5}$	0.50459	1428	1607×10^{-9}	0.79896
400	685.2	6138×10^{-7}	0.95869	429.2	$47\ 528 \times 10^{-6}$	0.646	1034	5586×10^{-9}	0.72454
420	463.3	$56\ 788 \times 10^{-7}$	0.98073	326.4	$33\ 432 \times 10^{-6}$	0.696	738.6	$10\ 148 \times 10^{-8}$	0.68974

decreasing slowly. The temperature dependent behavior of resistance is attributed to the increase of charge mobility and thus conduction process. As the rate of resistance decreases differently in each plot, the rate of conductance is also increasing differently which indicates different activation energies as previously seen. In fact, following the Arrhenius relation we have:

$$R = R_0 \exp\left(\frac{E_{ac}}{k_B T}\right) \quad (11)$$

where R_0 is a pre-exponential term, E_{ac} is the activation energy and k_B is the Boltzmann constant. Based on the plots given in Fig. 13

This law enables us to conclude two different activation energies in agreement with the results reported in the previous paragraphs.

Fig. 14 shows the variation of dielectric constant with frequency at various temperature ranging from 300 K to 400 K. As a matter of fact, we notice a giant permittivity of the order 10^6. In fact, the behavior of the permittivity could be divided according to the frequency. For low frequencies ($<10^3$ Hz) the real part of dielectric constant increases with temperature which indicates the thermal activation of the charge carriers and thus affects the polarization. In order to explain this trend, we resort to Maxwell–Wagner double layer model designed for inhomogeneous structures.[7,41]

We assume that the material is composed of two layers where the grains possess high conductance and grain boundaries have poor conductance. At lower frequencies the grain
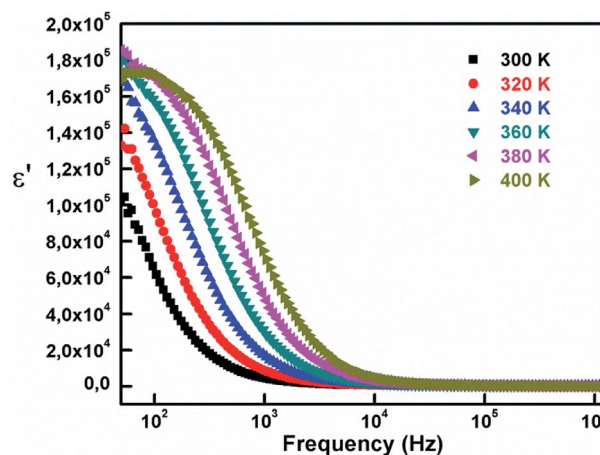
Fig. 14 Evolution of real part of dielectric permittivity (ε') as a function of frequency.

boundaries possess high resistance, so the electrons gather and generate polarization at the boundaries which explains the dielectric behavior of the material in the low frequency area. Thereafter we notice a rapid decrease of the dielectric constant independent of temperature. This could be attributed to the reverse electron motion as the frequency increase,[7] resulting in
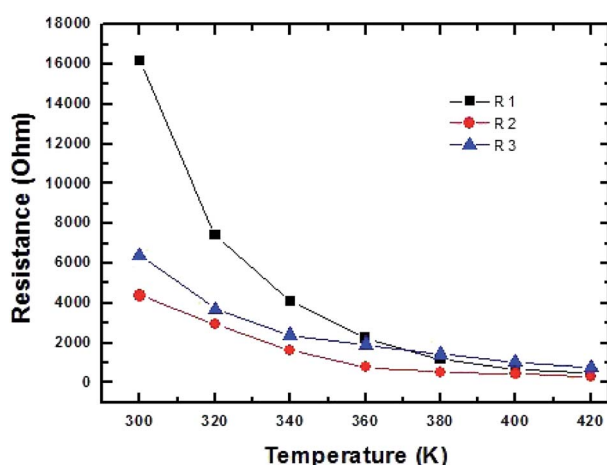
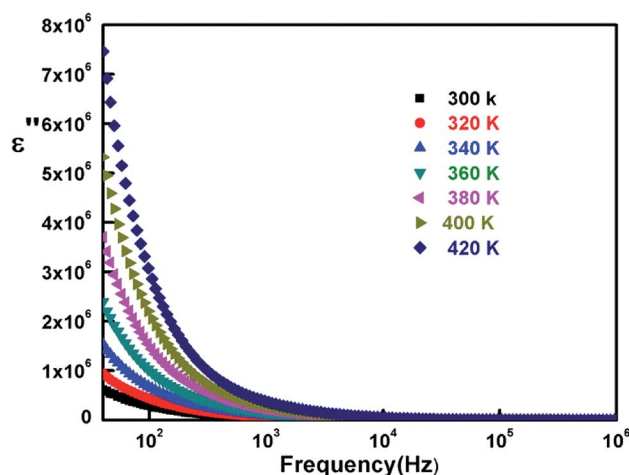**Fig. 13** Temperature dependence of resistance.

Fig. 15 Variation of imaginary part of dielectric constant with frequency at different temperatures.
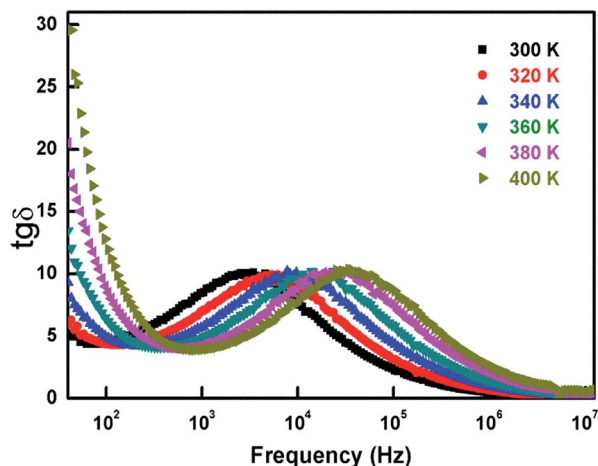
Fig. 16 Variation of dielectric loss tangent as a function of frequency at various temperatures.

reduction of polarization. We conclude that space-charge polarization is prominent in the first region. The variation of imaginary permittivity is presented in Fig. 15 as a function of frequency and at different temperatures.

The plots clearly show curves decreasing as the frequency rises. For the low frequency region, high dielectric constant values are ascribed to the highest temperatures and they diminish with it. As the frequency continues to rise, the dielectric constant also continues to lessen. Fig. 16 exhibits the frequency dependency of the dielectric tangent (tan δ) with varying temperature values. The plots show high loss for low frequency depending on temperatures, and then sharply decreases to a merging point between 10^2 Hz and 10^3 Hz.

The elevated resistance of grain boundaries at low frequencies results in electrons requiring high energy which justifies according to Koop's theory the high values of dielectric loss at that region.[43] In the following frequency region, up to 10^4 Hz the variation is reversed. We notice a light increase of dielectric loss that is more pronounced for lower temperatures reaching again a merging point. This behavior could be explained by the piling up of the electrons at the grain boundaries after reaching the area through hopping mechanism. The last region is defined by a similar behavior to that of the first one. There is a reduction of dielectric loss for the higher frequencies, and continues to gradually decrease tending towards zero irrespective to temperature. This coalescence is due to the poor energy loss during the exchange of electrons.

Conclusions

$Zn_{0.5}Ni_{0.5}FeO_4$ spinel ferrite is synthesized using the solid-state reaction technique. X-Ray diffractogramme reveals that our sample is pure and crystallizes in the orthorhombic system with *Pbnm* space group. The dielectric study is performed by complex impedance spectroscopy in a wide range of temperature [300–420 K] and frequency [40–10^7 Hz]. The relaxation frequency values are determined from impedance spectroscopy, which are thermally activated.

The evolution of ac conductance as a function of temperature and frequency is found to follow Maxwell–Wegner two-layer model.

Complex impedance plots have revealed the presence of tow semicircular arcs (grain and boundary grain). This behavior was modeled by an electrical equivalent circuit composed of three series sets of resistance and capacitance in parallel. Nyquist plots show two semicircles, revealing the presence of two relaxations processes in our material associated with grains and grain boundaries. Moreover, the real and imaginary part of dielectric constant were studied as a function both of temperature and frequency. The decrease of giant permittivity values with the increase in frequency proves the dispersion in low frequency range and is showing the Maxwell–Wagner interfacial polarization.

We note a light increase of dielectric loss. This behavior could be explained by the piling up of the electrons at the grain boundaries after reaching the area through hopping mechanism.

Conflicts of interest

There are no conflicts to declare.

References

1 M. K. Shobanaa, K. Kim and J. H. Kim, Impact of magnesium substitution in nickel ferrites: optical and electrochemical studies, *Phys. E*, 2019, **108**, 100–104.

2 M. Amiri, K. Eskandari and M. Salavati-Niasari, Magnetically retrievable ferrite nanoparticles in the catalysis application, *Adv. Colloid Interface Sci.*, 2019, **271**, 101982.

3 V. Uskokovic, M. Drofenik and I. Ban, The characterization of nanosized nickel–zinc ferrites synthesized within reverse micelles of CTAB/1–hexanol/water microemulsion, *J. Magn. Magn. Mater.*, 2004, **284**, 294–302.

4 Y. P. He, S. Q. Wang, C. R. Li, Y. M. Miao, Z. Y. Wu and B. S. Zou, Synthesis and characterization of functionalized silica-coated Fe_3O_4 superparamagnetic nanocrystals for biological applications, *J. Phys. D: Appl. Phys.*, 2005, **38**, 1342–1350.

5 Y. Ma, J. Fu, Z. Gao, L. Zhang, C. Li and T. Wang, Dicyclopentadiene Hydroformylation to Value-Added Fine Chemicals over Magnetically Separable Fe3O4-Supported Co–Rh Bimetallic Catalysts: Effects of Cobalt Loading, *Catalysts*, 2017, **7**, 103.

6 S. Mornet, S. Vasseur, F. Grasset, P. Veverka, G. Goglio, A. Demourgues, J. Portier, E. Pollert and E. Duguet, Magnetic nanoparticle design for medical applications, *Prog. Solid State Chem.*, 2006, **34**, 237–247.

7 M. Atif and M. Nadeem, Sol–gel synthesis of nanocrystalline $Zn_{1-x}Ni_xFe_2O_4$ ceramics and its structural, magnetic and dielectric properties, *J. Sol-Gel Sci. Technol.*, 2014, **72**, 615–626.

8 S. Deka and P. A. Joy, Enhanced permeability and dielectric constant of Ni–Zn ferrite synthesized in nanocrystalline form by a combustion method, *J. Am. Ceram. Soc.*, 2007, **90**, 1494–1499.

9 M. U. Islam, T. Abbas, S. B. Niazi, Z. Ahmad, S. Sabeen and M. A. Chaudhry, Electrical behavior of fine particle, co-

precipitation prepared Ni–Zn ferrites, *Solid State Commun.*, 2004, **130**, 353–356.

10 R. V. Mangalraja, S. Ananthakumar, P. Manohar and F. D. Gnanam, Dielectric behavior of $Ni_{1-x}Zn_xFe_2O_4$ prepared by flash combustion technique, *Mater. Lett.*, 2003, **57**, 1151–1155.

11 C. Upadhyay, D. Mishra, H. C. Verma, S. Anand and R. P. Das, Effect of preparation conditions on formation of nanophase Ni–Zn ferrites through hydrothermal technique, *J. Magn. Magn. Mater.*, 2003, **260**, 188–194.

12 N. M. Deraz and O. H. Abd-Elkader, Production and characterization of nano-magnetic $Ni_{0.5}Zn_{0.5}Fe_2O_4$ spinel solid solution, *J. Anal. Appl. Pyrolysis*, 2014, **106**, 171–176.

13 P. Sivakumar, R. Ramech, A. Ramanand, S. Ponnysamy and C. Muthamizhchelvan, Synthesis and characterization of $NiFe_2O_4$ nanoparticles and nanorods, *J. Alloys Compd.*, 2013, **563**, 6–11.

14 A. C. F. M. Costa, A. P. A. Diniz, A. G. B. de Melo, R. H. G. A. Kiminami, D. R. Cornejo, A. A. Costa and L. Gama, Ni–Zn–Sm nanopowder ferrites: Morphological aspects and magnetic properties, *J. Magn. Magn. Mater.*, 2008, **320**, 742–749.

15 K. Wu, J. Li and C. Zhang, Zinc ferrite based gas sensors : A review, *Ceram. Int.*, 2019, **45**, 11143–11157.

16 V. D. Kapse, S. A. Ghosh, F. C. Raghuwanshi and S. D. Kapse, Nanocrystalline spinel $Ni_{0.6}Zn_{0.4}Fe_2O_4$: A novel material for H_2S sensing, *Mater. Chem. Phys.*, 2009, **113**, 638–644.

17 V. G. Harris, Modern microwave ferrites, *IEEE Trans. Magn.*, 2012, **84**, 1075–1104.

18 J. S. Hardy, C. A. Coyle, J. F. Bonnett, J. W. Templeton, N. L. Canfield, D. J. Edwards, S. M. Mahserejian, L. Ge, B. J. Ingram and J. W. Stevenson, Evaluation of cation migration in lanthanum strontium cobalt ferrite solid oxide fuel cell cathodes *via* in-operando X-ray diffraction, *J. Mater. Chem. A*, 2018, **6**, 1787–1801.

19 R. Rani, G. Kumar, K. M. Batoo and M. Singh, Electric and Dielectric Study of Zinc Substituted Cobalt Nanoferrites Prepared by Solution Combustion Method, *Am. J. Nanomater.*, 2013, **1**, 9–12.

20 H. Parmar, R. V. Upadhyay, S. Rayaprol and V. Siruguri, Structural and magnetic properties of nickel–zinc ferrite nanocrystalline magnetic particles prepared by microwave combustion method, *Indian J. Phys.*, 2014, **88**, 1257–1264.

21 P. P. Hankare, U. Sankpal, R. Patil, I. Mulla, R. Sasikala, A. Tripathi and K. Garadkar, Synthesis and characterization of nanocrystalline zinc substituted nickel ferrites, *J. Alloys Compd.*, 2010, **496**, 256–260.

22 N. Gupta, A. Verma, S. C. Kashyap and D. C. Dube, Dielectric behavior of spin deposited nanocrystalline nickel–zinc ferrite thin films processed by citrate-route, *Solid State Commun.*, 2005, **134**, 689–694.

23 H. Rahmouni, A. Benali, B. Cherif, E. Dhahri, M. Boukhobza, K. Khirouni and M. Sajieddine, Structural and electrical properties of $Zn_{1-x}Ni_xFe_2O_4$ ferrite, *Phys. B*, 2015, 31–37.

24 H. M. Rietveld, A profile refinement method for nuclear and magnetic structures, *J. Appl. Crystallogr.*, 1965, **2**, 65–71.

25 *Théorie et Technique de la radiocristallographie*, ed. A. Guinier and X. Dunod, 3rd edn, 1964, p. 462.

26 J. Sharma, J. Parashar, V. K. Saxena, D. Bhatnagar and K. B. Sharma, Study of dielectric properties of nanocrystalline cobalt ferrite up to microwave frequencies, *Macromol. Symp.*, 2015, **357**, 38–42.

27 S. Mollah, K. K. Som, K. Bose and B. K. Chaudri, *J. Appl. Phys.*, 1993, **74**, 931.

28 S. A. Mazen and A. M. El Taher, The conduction mechanism of Cu–Ge ferrite, *Solid State Commun.*, 2010, **150**, 1719–1724.

29 N. F. Mott and E. A. Davis, *Electronic processes in non-crystalline materials*, Clarendon Press/Oxford University press, 2nd edn, 1979.

30 S. A. Mazen and A. M. El Taher, The conduction mechanism of Cu–Si ferrite, *J. Alloys Compd.*, 2010, **498**, 19–25.

31 B. Kumar, Ceramic nanocomposites for energy storage and power generation, *Ceramic Nanocomposites*, 2013, 509–529.

32 L. S. Lobo and A. B. Kumar, Structural and electrical properties of $ZnCo_2O_4$ spinel synthesized by sol–gel combustion method, *J. Non- Cryst. Solids*, 2019, **505**, 301–309.

33 F. Borsa, D. R. Torgeson, S. W. Martin and H. K. Patel, Relaxation and fluctuations in glassy-fast-ion conductors : Wide-frequency-range NMR and conductivity measurements, *Phys. Rev. B: Condens. Matter Mater. Phys.*, 1992, **46**, 795.

34 E. V. Ramana, S. V. Suryanarayana and T. B. Sankaram, Ac impedance studies of ferro electromagnetic $SrBi_{5-x}La_xTi_4FeO_{18}$ ceramics, *Mater. Res. Bull.*, 2006, **41**, 1077–1088.

35 A. Omri, M. Bejar, E. Dhahri, M. Es-Souni, M. A. Valente, M. P. F. Graça and L. C. Costa, Electrical conductivity and dielectric analysis of $La_{0.75}(Ca,Sr)_{0.25}Mn_{0.85}Ga_{0.15}O_3$ perovskite compound, *J. Alloys Compd.*, 2012, **536**, 173–178.

36 M. A. Valente, *Opt. Mater.*, 2001, **33**, 1964.

37 N. V. Prasad, C. S. Manda and G. S. Kumar, Impedance spectroscopic studies on lead based perovskite materials, *Ferroelectrics*, 2008, **366**, 55–66.

38 S. Lily, K. Kumari, K. Prasad and R. N. P. Choudhary, Impedance spectroscopy of $(Na_{0.5}Bi_{0.5})(Zr_{0.25}Ti_{0.75})O_3$ lead-free ceramic, *J. Alloys Compd.*, 2008, **453**, 325–331.

39 K. Ashok, M. B. Suresh and P. Sarah, Electrical properties of Li and Nd doped $SrBi_4Ti_4O_{15}$ ceramics, *Int. J. Pure Appl. Res. Eng. Technol.*, 2013, **2**, 3299–3307.

40 K. S. Cole and R. H. Cole, Dispersion and Absorption in Dielectrics I. Alternating Current Characteristics, *J. Chem. Phys.*, 1941, **9**, 341.

41 L. S. Lobo and A. B. Kumar, Structural and electrical properties of $ZnCo_2O_4$ spinel synthesized by sol-gel combustion method, *J. Non-Cryst. Solids*, 2019, **505**, 301–309.

42 E. Barsoukov and J. R. Macdonald, *Impedance Spectroscopy theory, Experiment and Applications*, 2nd edn, 2005, p. 18.

43 A. K. Roy, K. Prasad and A. Prasad, Piezoelectric, impedance, electric modulus and Ac conductivity studies on $(Bi_{0.5}Na_{0.5})_{0.95}Ba_{0.05}TiO_3$ ceramic, *Process. Appl. Ceram.*, 2013, **7**, 81–91.